symmetry

MDPI

Article

D-Wave Superconducting Gap Symmetry as a Model for $Nb_{1-x}Mo_xB_2$ (x = 0.25; 1.0) and WB_2 Diborides

Evgeny F. Talantsev [1,2]

[1] M. N. Miheev Institute of Metal Physics, Ural Branch, Russian Academy of Sciences, 18, S. Kovalevskoy St., Ekaterinburg 620108, Russia; evgeny.talantsev@imp.uran.ru; Tel.: +7-912-676-0374
[2] NANOTECH Centre, Ural Federal University, 19 Mira St., Ekaterinburg 620002, Russia

Abstract: Recently, Pei et al. (*National Science Review* **2023**, *nwad034*, 10.1093/nsr/nwad034) reported that ambient pressure β-MoB_2 (space group: $R\bar{3}m$) exhibits a phase transition to α-MoB_2 (space group: $P6/mmm$) at pressure P~70 GPa, which is a high-temperature superconductor exhibiting $T_c = 32$ K at P~110 GPa. Although α-MoB_2 has the same crystalline structure as ambient-pressure MgB_2 and the superconducting critical temperatures of α-MoB_2 and MgB_2 are very close, the first-principles calculations show that in α-MoB_2, the states near the Fermi level, ε_F, are dominated by the d-electrons of Mo atoms, while in MgB_2, the p-orbitals of boron atomic sheets dominantly contribute to the states near the ε_F. Recently, Hire et al. (*Phys. Rev. B* **2022**, *106*, 174515) reported that the $P6/mmm$-phase can be stabilized at ambient pressure in $Nb_{1-x}Mo_xB_2$ solid solutions, and that these ternary alloys exhibit $T_c \sim 8$ K. Additionally, Pei et al. (*Sci. China-Phys. Mech. Astron.* **2022**, *65*, 287412) showed that compressed WB_2 exhibited $T_c \sim 15$ K at P~121 GPa. Here, we aimed to reveal primary differences/similarities in superconducting state in MgB_2 and in its recently discovered diboride counterparts, $Nb_{1-x}Mo_xB_2$ and highly-compressed WB_2. By analyzing experimental data reported for *P6/mmm*-phases of $Nb_{1-x}Mo_xB_2$ (x = 0.25; 1.0) and highly compressed WB_2, we showed that these three phases exhibit *d*-wave superconductivity. We deduced $\frac{2\Delta_m(0)}{k_B T_c} = 4.1 \pm 0.2$ for α-MoB_2, $\frac{2\Delta_m(0)}{k_B T_c} = 5.3 \pm 0.1$ for $Nb_{0.75}Mo_{0.25}B_2$, and $\frac{2\Delta_m(0)}{k_B T_c} = 4.9 \pm 0.2$ for WB_2. We also found that $Nb_{0.75}Mo_{0.25}B_2$ exhibited high strength of nonadiabaticity, which was quantified by the ratio of $\frac{T_\theta}{T_F} = 3.5$, whereas MgB_2, α-MoB_2, and WB_2 exhibited $\frac{T_\theta}{T_F} \sim 0.3$, which is similar to the $\frac{T_\theta}{T_F}$ in pnictides, A15 alloys, Heusler alloys, Laves phase compounds, cuprates, and highly compressed hydrides.

Keywords: superconducting diborides; superconducting gap symmetry; high-pressure superconductivity; nonadiabatic superconductors

Citation: Talantsev, E.F. *D*-Wave Superconducting Gap Symmetry as a Model for $Nb_{1-x}Mo_xB_2$ (x = 0.25; 1.0) and WB_2 Diborides. *Symmetry* **2023**, *15*, 812. https://doi.org/10.3390/sym15040812

Academic Editors: Heshan Yu and Ge He

Received: 4 March 2023
Revised: 20 March 2023
Accepted: 23 March 2023
Published: 27 March 2023

1. Introduction

There is an experimental quest for high-temperature superconductivity in compounds based on lightweight elements which exhibit high Debye temperature, T_θ. Thus, in accordance with the theory of the electron–phonon mediated superconductivity, these compounds can have a high transition temperature, T_c. This work started in the 1970s [1,2]. These studies covered hydrides [1] and borides [2]. Surprisingly, Cooper et al. [2] performed detailed studies of Mo-diborides, Nb-diborides, and ternary borides $R_{2-x}A_xB_5$ (R = Mo, Nb, A = transition metal), while Fisk [3] reported on discovery of 40 superconducting phases in rare earth and transition metals borides. The diboride of magnesium was first studied on its superconducting properties in 2001 [4].

The discovery of near-room temperature superconductivity in highly compressed sulfur hydride by Drozdov et al. [5] sparked theoretical and experimental studies of a variety of materials that can potentially exhibit high-temperature superconductivity to be compressed at high pressure [6–29]. This research field represents one of the most fascinating scientific explorations in which advanced first-principles calculations are combined with the top world class of experimental studies [30–43].

In this regard, the quest for high-temperature superconductivity in highly compressed borides seems reasonable. One of the interesting results of this conjunctive exploration was reported by Pei et al. [44], who found that the stoichiometric compound MoB_2 exhibits a phase transition from the β-MoB_2-phase (space group: $R\bar{3}m$) to the α-MoB_2-phase (space group: $P6/mmm$) at a critical pressure of P~70 GPa. This high-pressure phase, α-MoB_2, exhibits the same crystalline structure as the ambient-pressure MgB_2. The most intriguing experimental result reported by Pei et al. [44] was that the α-MoB_2 phase is a high-temperature superconductor with $T_c = 32$ K (at P = 109.7 GPa); this value is remarkably close to $T_c = 39 - 42$ K in MgB_2 [4,45].

First-principles calculations performed by Pei et al. [44] showed that several bands in the α-MoB_2 cross the Fermi level, ε_F, which causes the metallic type of conductivity in this phase. Pei et al. [44] also showed that molybdenum d-orbitals (especially the d_{z2} orbital) have larger contributions than boron p-orbitals near the ε_F. Overall, although the α-MoB_2 phase exhibits the same crystal structure as MgB_2 and the superconducting transition temperatures for these compounds are comparable, their electronic structures are different. For instance, the out-of-plane phonon mode of molybdenum ions is strongly coupled with molybdenum d-electrons near the ε_F in α-MoB_2 [44], whereas the in-plane B-B stretching mode in MgB_2 interacts intensively with the σ-bond in the boron honeycomb lattice near the ε_F [44]. Pei et al. [44] also calculated the electron–phonon coupling constant, $\lambda_{e-ph} = 1.60$, in α-MoB_2 at $P = 90$ GPa. Similar findings, including $\lambda_{e-ph} = 1.60$, were reported by Quan et al. [46], who performed first-principles calculations for a highly pressurized α-MoB_2 phase.

These results establish a ground to expect that the α-MoB_2 phase can exhibit d-wave superconducting energy gap symmetry (or, at least, s+d-wave gap symmetry with a significant d-wave component), which is different from the two-band s-wave MgB_2.

More recently, Hire et al. [47] showed that the $P6/mmm$-phase can be stabilized at ambient pressure in $Nb_{1-x}Mo_xB_2$ (x = 0.25, 0.50, 0.75, and 0.9) solid solutions. Despite the superconducting transition temperature in $Nb_{1-x}Mo_xB_2$ (x = 0.25, 0.50, 0.75 and 0.9) being significantly lower (i.e., $T_c = (6.5 - 8.1)$ K [47]), these values are still high enough to suggest that the same pairing mechanism emerges in ambient pressure superconductors $Nb_{1-x}Mo_xB_2$ and highly-pressurized α-MoB_2.

Hire et al. [47] also performed first-principles calculations and measured the temperature-dependent magnetoresistance, $R(T, B)$, and specific heat, from which several parameters of $Nb_{1-x}Mo_xB_2$ (x = 0.25, 0.50, 0.75, and 0.9) superconductors (in particular, the Debye temperature, T_θ) were determined.

Pei et al. [48] and Lim et al. [49] extended the family of superconducting diborides by the discovery of the highly compressed phase of WB_2 ($T_c \sim 15$ K at P~121 GPa) for which Pei et al. [48] proposed the space group: $P6_3/mmc$ (which is distorted $P6/mmm$), while Lim et al. [49] concluded that this highly pressurized superconducting phase of WB_2 formed by stacking faulted $P6_3/mmc$-$P6/mmm$ phases (which can be found to be similar to the stacking faulted 123–124 phases in the Y-Ba-Cu-O system [50–52]).

Here, we aimed to determine the difference in the superconducting gap symmetry and other superconducting parameters in MgB_2 and in the recently discovered $Nb_{1-x}Mo_xB_2$ (x = 0.25; 1.0) and WB_2, which might originate from the difference in the band structure of these materials. To do this we performed a detailed analysis of the magnetoresistance data reported by Pei et al. [44], Hire et al. [47], and Pei et al. [48] and showed that the $P6/mmm$-phases of $Nb_{1-x}Mo_xB_2$ (x = 0.25, 1.0) and WB_2 (P = 121.3 GPa) exhibit d-wave superconducting gap symmetry. We also found that ambient pressure $Nb_{1-x}Mo_xB_2$ (x = 0.25) superconductors characterized by high strength of nonadiabaticity, which can be characterized by the ratio of $\frac{T_\theta}{T_F} = 3.5$ (where T_F is the Fermi temperature, which exceeds the $\frac{T_\theta}{T_F}$ ratio in MgB_2, α-MoB_2, WB_2, pnictides, A15 alloys, Heusler alloys, Laves phase compounds, cuprates, and highly-compressed hydrides by more than one order of magnitude.

2. Utilized Models

The Debye temperature, T_θ, can be deduced from the fit of the experimentally measured temperature-dependent resistance curve, $R(T)$, to the Bloch–Grüneisen (BG) equation [53,54]. In many reports, the classical BG approach was advanced by introducing the so-called saturation resistance [55–60]:

$$R(T) = \frac{1}{\frac{1}{R_{sat}} + \frac{1}{R_0 + A\left(\frac{T}{T_\theta}\right)^5 \int_0^{\frac{T_\theta}{T}} \frac{x^5}{(e^x-1)(1-e^{-x})} dx}}, \quad (1)$$

where R_{sat}, R_0, T_θ, and A are free fitting parameters. From the deduced T_θ and measured T_c (which we defined by as strict as practically possible resistance criterion of $\frac{R(T)}{R_{norm}} \to 0$, where R_{norm} is the normal state resistance at the onset of the superconducting transition (ee details in [59]), the electron–phonon coupling constant, λ_{e-ph}, can be calculated as the unique root of the advanced McMillan equation [59]:

$$T_c = \left(\frac{1}{1.45}\right) \times T_\theta \times e^{-\left(\frac{1.04(1+\lambda_{e-ph})}{\lambda_{e-ph}-\mu^*(1+0.62\lambda_{e-ph})}\right)} \times f_1 \times f_2^*, \quad (2)$$

where

$$f_1 = \left(1 + \left(\frac{\lambda_{e-ph}}{2.46(1+3.8\mu^*)}\right)^{3/2}\right)^{1/3}, \quad (3)$$

$$f_2^* = 1 + (0.0241 - 0.0735 \times \mu^*) \times \lambda_{e-ph}^2, \quad (4)$$

where μ^* is the Coulomb pseudopotential parameter, which we assumed (following the approach proposed in [44,47,49]) to be $\mu^* = 0.13$ for $Nb_{1-x}Mo_xB_2$ (x = 0.25; 1.0) and WB_2.

By following the general logic [59,61,62] that a resistance criterion with the smallest possible value should be in use, we utilized the same criterion of $\frac{R(T)}{R_{norm}(T)} = 0.10$, as the one that was used to define the T_c and the $B_{c2}(T)$. The temperature-dependent upper critical field, $B_{c2}(T)$, is described by

$$B_{c2}(T) = \frac{\phi_0}{2 \cdot \pi \cdot \xi^2(T)}, \quad (5)$$

where ϕ_0 is the superconducting magnetic flux quantum and $\xi(T)$ is the coherence length. $B_{c2}(T)$ datasets were fitted to the equation for the temperature-dependent upper critical field for *s*-wave superconductors [61–63]:

$$B_{c2}(T) = \frac{\phi_0}{2 \cdot \pi \cdot \xi^2(0)} \left(\frac{1.77 - 0.43\left(\frac{T}{T_c}\right)^2 + 0.07\left(\frac{T}{T_c}\right)^4}{1.77}\right)^2 \times \left[1 - \frac{1}{2k_BT}\int_0^\infty \frac{d\varepsilon}{cosh^2\left(\frac{\sqrt{\varepsilon^2+\Delta^2(T)}}{2k_BT}\right)}\right], \quad (6)$$

where the amplitude of the temperature-dependent superconducting gap, $\Delta(T)$, is given by [64,65]

$$\Delta(T) = \Delta(0) \times \tanh\left[\frac{\pi k_B T_c}{\Delta(0)}\sqrt{\eta \frac{\Delta C}{\gamma T_c}\left(\frac{T_c}{T} - 1\right)}\right], \quad (7)$$

where $\eta = 2/3$ for *s*-wave superconductors, γ is the Sommerfeld constant, and k_B is Boltzmann's constant.

$B_{c2}(T)$ datasets were also fitted to the equation for the temperature-dependent upper critical field for *d*-wave superconductors [61–63], where the amplitude of the temperature-dependent superconducting gap, $\Delta(T)$, is given by [64,65]:

$$B_{c2}(T) = \frac{\phi_0}{2\cdot\pi\cdot\xi^2(0)}\left(\frac{1.77-0.43\left(\frac{T}{T_c}\right)^2+0.07\left(\frac{T}{T_c}\right)^4}{1.77}\right)^2\left[1-\frac{1}{2\cdot k_B\cdot T}\cdot\right.$$
$$\left.\int_0^{2\pi} cos^2(\theta)\cdot\left(\int_0^{\infty}\frac{d\varepsilon}{cosh^2\left(\frac{\sqrt{\varepsilon^2+\Delta^2(T,\theta)}}{2\cdot k_B\cdot T}\right)}\right)\cdot d\theta\right], \quad (8)$$

where the superconducting energy gap, $\Delta(T,\theta)$, is given by [64–67]:

$$\Delta(T,\theta) = \cos(2\theta)\times\Delta_m(0)\times\tanh\left[\frac{\pi k_B T_c}{\Delta(0)}\sqrt{\eta\frac{\Delta C}{\gamma T_c}\left(\frac{T_c}{T}-1\right)}\right], \quad (9)$$

where $\Delta_m(0)$ is the maximum amplitude of the *k*-dependent *d*-wave gap, $\eta = 7/5$ [68], θ is the angle around the Fermi surface subtended at (π,π) in the Brillouin zone (details can be found elsewhere [64,65]).

The Fermi temperature, T_F, was calculated using the equation [61]:

$$T_F = \frac{\pi^2 m_e}{8\cdot k_B}\times\left(1+\lambda_{e-ph}\right)\times\xi^2(0)\times\left(\frac{2\Delta_m(0)}{\hbar}\right)^2, \quad (10)$$

where m_e is the bare electron mass, $\hbar$ is the reduced Planck's constant, and the other parameters were deduced above.

3. Results

3.1. P6/mmm α-MoB$_2$ (P = 109.7 GPa)

The fits of $R(T)$ datasets, measured for the α-MoB_2 phase at $P = 91.4$ and 109.7 GPa [44] of Equation (1), together with the deduced R_{sat}, T_θ, and λ_{e-ph}, are shown in Figure 1 (where we utilized $\frac{R(T)}{R_{norm}(T)} = 0.10$ criterion to define T_c because the same criterion was used by Pei et al. [44] to define the upper critical field in the same α-MoB_2 sample).

The deduced $\lambda_{e-ph}(91.4\text{ GPa}) = 1.42$ is in good agreement with the value calculated by first-principles calculations, $\lambda_{e-ph}(90\text{ GPa}) = 1.60$ [44,46].

In Figure 2a, the $B_{c2}(T)$ dataset is fitted to the equation for the temperature-dependent upper critical field for *s*-wave superconductors (Equations (6) and (7)). However, the deduced $\frac{2\Delta(0)}{k_B T_c} = 2.3\pm0.1$ (Figure 2a) is too low to be attributed to *s*-wave superconductivity, for which the weak-coupling limit is $\frac{2\Delta(0)}{k_B T_c} = 3.53$ [66,67]. Additionally, the fit quality was low (coefficient of determination = 0.8267).

Subsequently, we fitted the temperature-dependent upper critical field data to the *d*-wave gap symmetry model. The fit converged with a better quality (goodness of fit of 0.9842) (Figure 2b). The deduced parameters are $\xi(0) = 6.2(5)$ nm, $\Delta(0) = 5.0\pm0.2$ meV, $\frac{2\Delta(0)}{k_B T_c} = 4.1\pm0.2$, $\frac{\Delta C}{\gamma T_c} = 0.8\pm0.1$. Considering that the weak coupling limits for *d*-wave superconductors [64–66] are $\frac{2\cdot\Delta(0)}{k_B\cdot T_c} = 4.28$ and $\frac{\Delta C}{\gamma T_c} = 0.995$, we can conclude that the deduced parameters in α-MoB_2 ($P = 109.7$ GPa) superconductor are within the weak-coupling values for *d*-wave superconductors.

It should be noted that the accuracy of the extracted parameters is directly related to the sampling number of the measurement. Thus, further increase in the accuracy of the deduced parameters is possible if more raw $R(T,B)$ data (especially, measured at low temperatures, down to the milliKelvin level) are available.

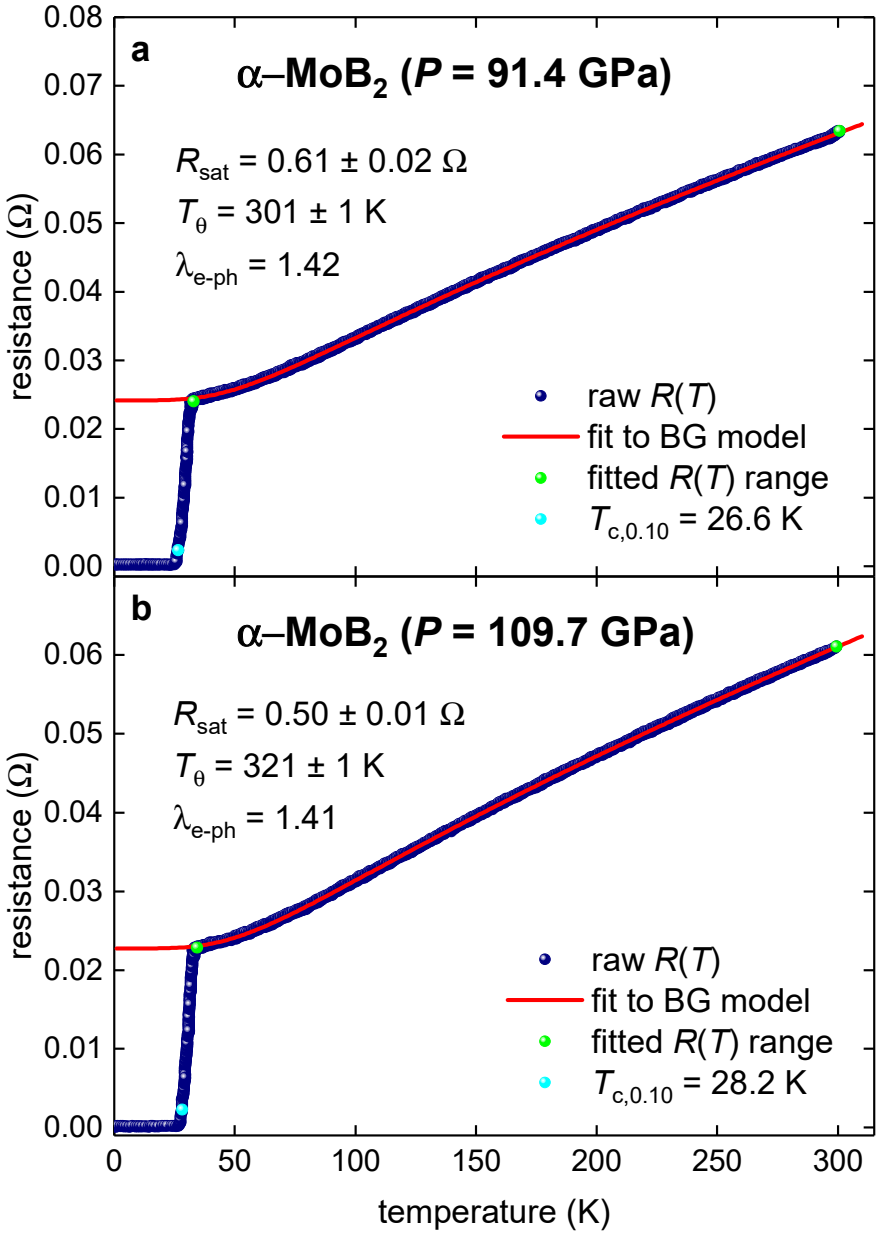

Figure 1. $R(T)$ data for highly compressed α-MoB_2 (P = 109.7 GPa) and data fit to Equation (1) (raw data reported by Pei et al. [44]). The green balls indicate the bounds for which $R(T)$ data were used to fit data to Equation (1). (**a**) Deduced $T_\theta = 301 \pm 1$ K, $T_{c,0.10} = 26.6$ K, $\lambda_{e-ph} = 1.42$, $R_{sat} = 0.61 \pm 0.02$ Ω, fit quality is 0.9998. (**b**) Deduced $T_\theta = 321 \pm 1$ K, $T_{c,0.10} = 28.2$ K, $\lambda_{e-ph} = 1.41$, $R_{sat} = 0.50 \pm 0.01$ Ω; fit quality is 0.9998. The 95% confidence bands are indicated by pink shadowed areas.

From the deduced parameters, one can calculate the Fermi temperature $T_F = 1756 \pm 25$ K. The calculated T_F implies that the *P6/mmm* α-MoB_2 ($P = 109.7$ GPa) phase falls in the unconventional superconductor band in the Uemura plot (Figure 3) because this phase is typical for many unconventional superconductors (for instance, iron-based, cuprates, and hydrogen-rich superconductors) ratio of $\frac{T_c}{T_F} = 0.016$. Raw data for this plot were reported by many research groups (Refs. [68–78]).

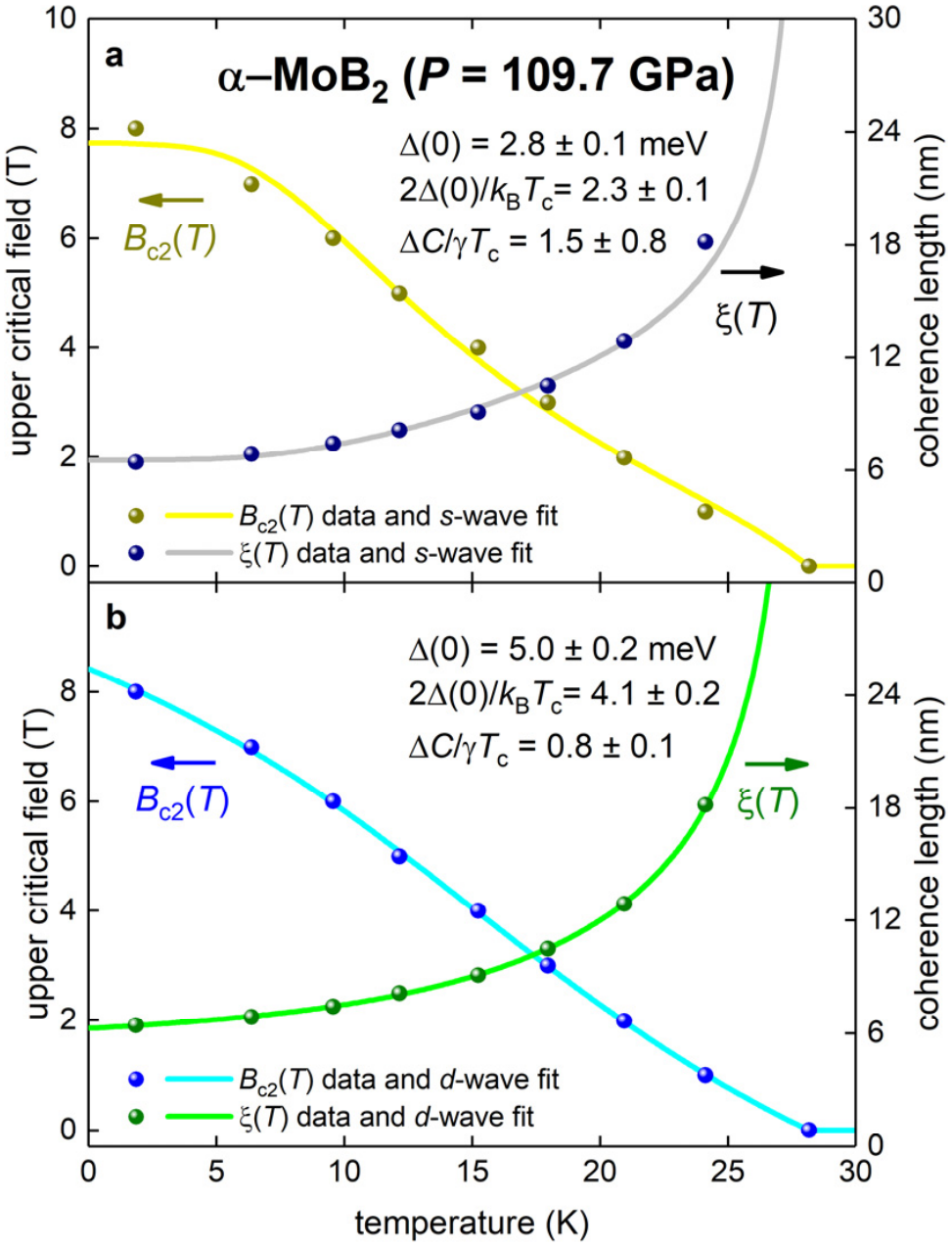

Figure 2. Temperature-dependent upper critical field, $B_{c2}(T)$, and data (left Y-axes) (defined by $\frac{R(T)}{R_{norm}(T)} = 0.10$ criterion), calculated by Equation (5). The coherence length $\xi(T)$ (right Y-axes) for α-MoB_2 ($P = 109.7$ GPa) reported by Pei et al. [44] and data fits to *s*-wave (panel **a**) and *d*-wave (panel **b**) single-band models. Deduced parameters are (for both panels the critical temperature was fixed to the observed value of T_c = 28.2 K): (**a**) *s*-wave fit, $\xi(0) = 6.5(2)$ nm, $\Delta(0) = 2.8 \pm 0.1$ meV, $\Delta C/\gamma T_c = 1.5 \pm 0.8$, $\frac{2\Delta(0)}{k_B T_c} = 2.3 \pm 0.2$, the goodness of fit is 0.8267; (**b**) *d*-wave fit, $\xi(0) = 6.2(5)$ nm, $\Delta(0) = 5.0 \pm 0.2$ meV, $\Delta C/\gamma T_c = 0.8 \pm 0.1$, $\frac{2\Delta(0)}{k_B T_c} = 4.1 \pm 0.2$, the goodness of fit is 0.9842.

In addition, we found that the *P6/mmm* α-MoB_2 ($P = 109.7$ GPa) phase exhibits a similar level of nonadiabaticy ($\frac{T_\theta}{T_F} = 0.18 \pm 0.02$) to iron-based, cuprates, and hydrogen-rich superconductors [69,70] (Figures 4 and 5).

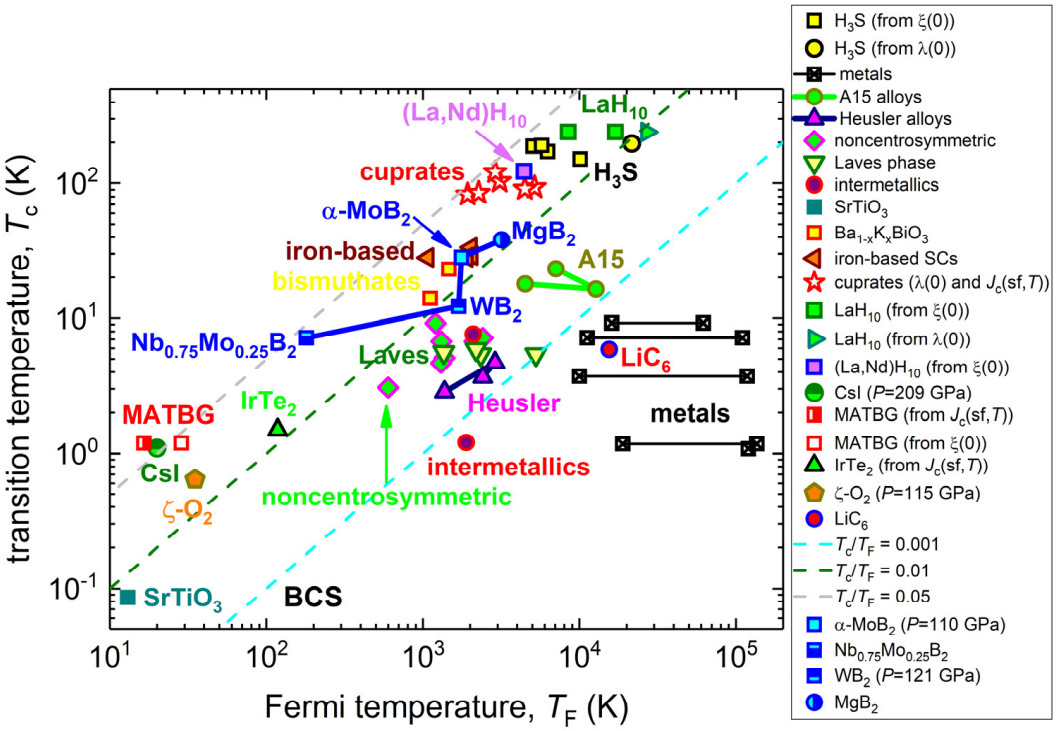

Figure 3. Uemura plot (T_c vs. T_F), where the diborides are shown together with other superconducting families: 2D materials, metals, pnictides, cuprates, and near-room-temperature superconductors. References to the original data can be found in Refs. [68–78].

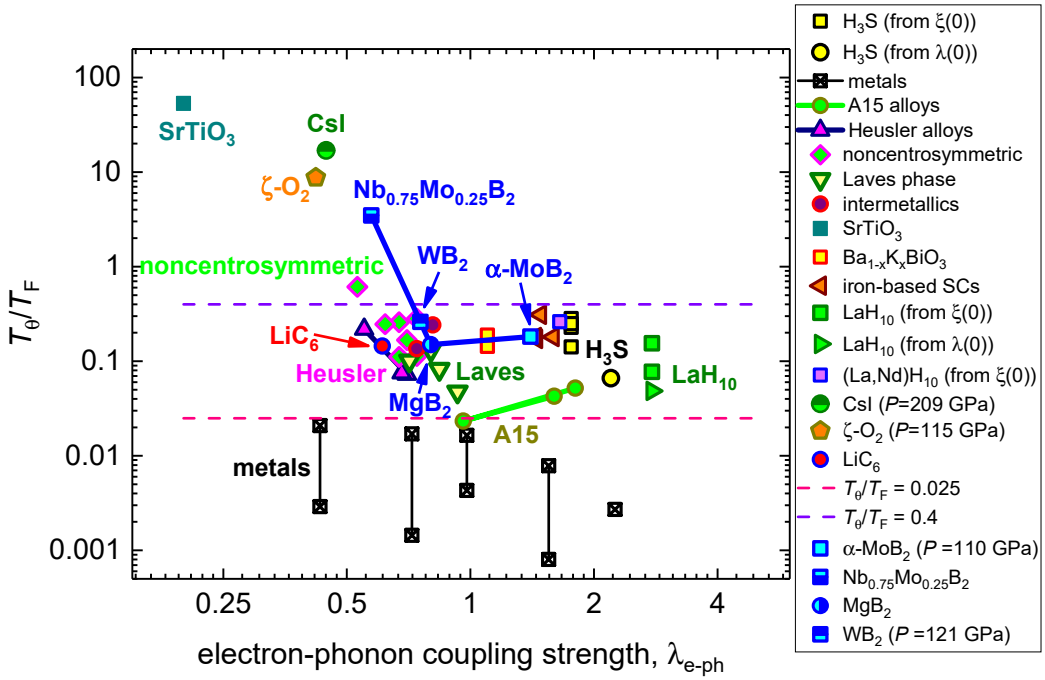

Figure 4. Plot of $\frac{T_\theta}{T_F}$ vs. λ_{e-ph} for several superconducting families and diborides. This type of plot was proposed by Pietronero et al. [69]. References to the original data can be found in Refs. [68–74]. In this plot, we assumed that α-MoB_2, WB_2, and the $Nb_{1-x}Mo_xB_2$ ($x = 0.25$) exhibit the Coulomb pseudopotential parameter, $\mu^* = 0.13$.

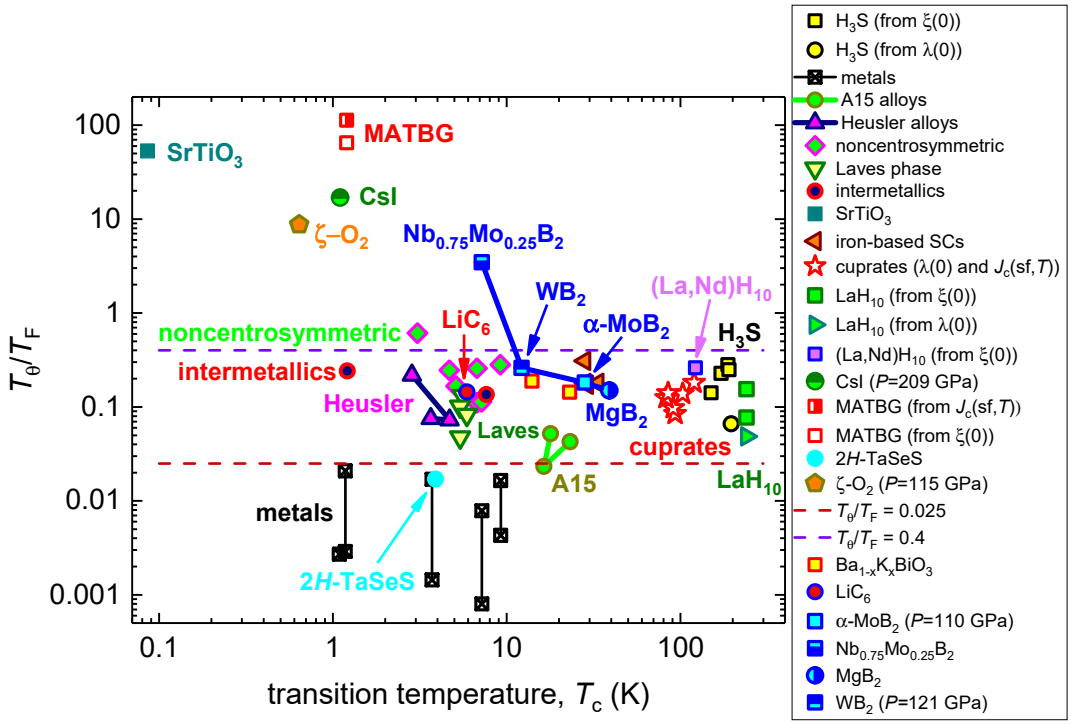

Figure 5. Plot of $\frac{T_\theta}{T_F}$ vs. T_c for several superconducting families and diborides. References to the original data can be found in Refs. [68,70–75].

3.2. Ambient Pressure P6/mmm $Nd_{0.75}Mo_{0.25}B_2$

In Table 1 of Hire et al.'s work [24], they reported the Debye temperature for *P6/mmm* $Nb_{1-x}Mo_xB_2$ ($x = 0.25$), which was deduced from low-temperature specific heat measurements, $T_\theta = 625$ K. Following the approach implemented in this study, we processed $R(T, B = 0)$ data reported by Hire et al. [24] by utilizing the resistance criterion of $\frac{R(T)}{R_{norm}(T)} = 0.015$. We deduced $T_{c,0.015} = 7.2$ K, from which $\lambda_{e-ph} = 0.573$ was calculated using Equations (2)–(4).

In Figure 6 of Hire et al. [47]'s work, they reported $R(T, B)$ data, which we processed by utilizing the resistance criterion of $\frac{R(T)}{R_{norm}(T)} = 0.015$. We deduced the $B_{c2}(T)$ dataset. The fits of this dataset to the *s*-wave (Equations (6) and (7)) and *d*-wave model (Equations (8) and (9)) are shown in Figure 6.

The deduced parameters for *s*-wave (Figure 6a) contradict each other, i.e., $\frac{2\Delta(0)}{k_B T_c} = 3.18 \pm 0.15$ (which is lower than the *s*-wave weak-coupling limit is $\frac{2\Delta(0)}{k_B T_c} = 3.53$ [66,67]). The deduced $\frac{\Delta C}{\gamma T_c} = 1.62 \pm 0.19$ is larger than the *s*-wave weak-coupling limit of $\frac{\Delta C}{\gamma T_c} = 1.43$. The fit quality is not high and has a coefficient of determination of 0.9534.

The fit to the *d*-wave gap symmetry model has a better quality (with a goodness of fit of 0.9959) (Figure 6b). The deduced parameters are $\xi(0) = 6.2(5)$ nm, $\Delta(0) = 1.65 \pm 0.05$ meV, $\frac{2\Delta(0)}{k_B T_c} = 5.3 \pm 0.1$, and $\frac{\Delta C}{\gamma T_c} = 1.13 \pm 0.03$; these values characterize the material as being a moderately strong coupled *d*-wave superconductor (considering that the weak coupling limits for *d*-wave superconductors [64–66] are $\frac{2 \cdot \Delta(0)}{k_B \cdot T_c} = 4.28$ and $\frac{\Delta C}{\gamma T_c} = 0.995$). It should be noted that analyzed experimental $B_{c2}(T)$ dataset has six raw data points which cover the $0.2 \leq \frac{T}{T_c} \leq 1.0$ range. More experimental $B_{c2}(T)$ data measured at wider temperature ranges can be used to deduce primary superconducting parameters of the $Nb_{0.75}Mo_{0.25}B_2$ with better accuracy.

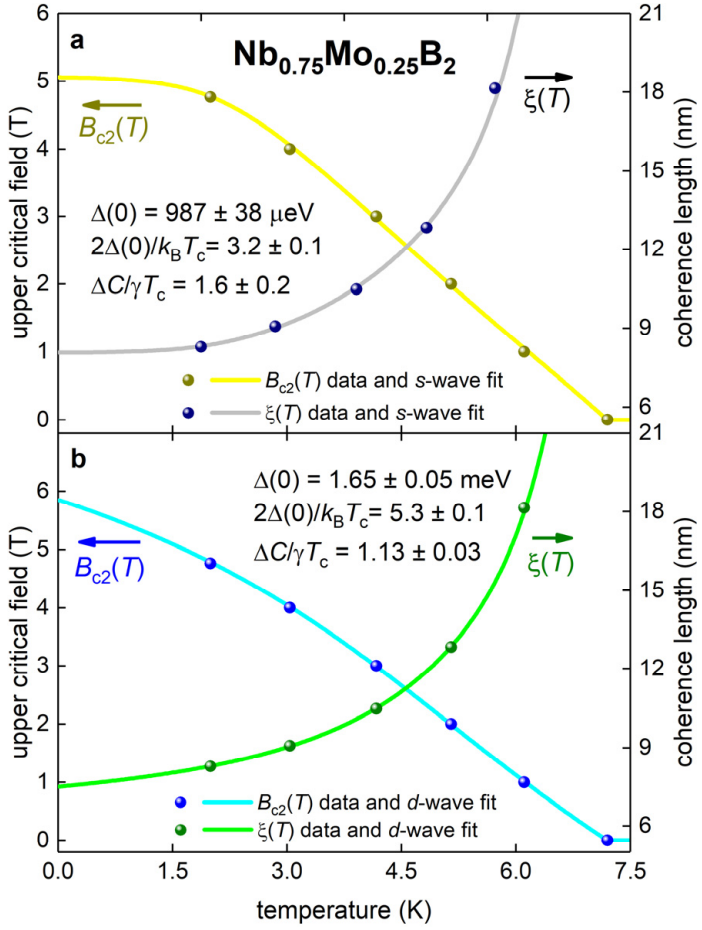

Figure 6. Temperature dependent upper critical field, $B_{c2}(T)$, data (left Y-axes) (defined by $\frac{R(T)}{R_{norm}(T)} = 0.015$ criterion) and calculated by Equation (5). The coherence length $\xi(T)$ (right Y-axes) for *P6/mmm* $Nb_{0.75}Mo_{0.25}B_2$ reported by Hire et al. [47], and data fit to *s*-wave (panel **a**) and *d*-wave (panel **b**) single-band models. Deduced parameters are (for both panels the critical temperature was fixed to the observed value of T_c = 7.2 K) (**a**) *s*-wave fit, $\xi(0) = 8.0(7)$ nm, $\Delta(0) = 0.987 \pm 0.038$ meV, $\Delta C/\gamma T_c = 1.6 \pm 0.2$, $\frac{2\Delta(0)}{k_B T_c} = 3.2 \pm 0.1$, the goodness of fit is 0.9534; (**b**) *d*-wave fit, $\xi(0) = 7.5(0)$ nm, $\Delta(0) = 1.65 \pm 0.05$ meV, $\Delta C/\gamma T_c = 1.13 \pm 0.03$, $\frac{2\Delta(0)}{k_B T_c} = 5.3 \pm 0.1$, the goodness of fit is 0.9959.

By the substituting the deduced parameters in Equation (10), the Fermi temperature can be obtained: $T_F = 180 \pm 7$ K in *P6/mmm*-phase of $Nb_{0.75}Mo_{0.25}B_2$. The calculated T_F implies that this phase falls in the unconventional superconductors band in the Uemura plot (Figure 3) because this phase is typical for many unconventional superconductor ratios of $\frac{T_c}{T_F} = 0.042$.

However, what comes from our analysis and reported by Hire et al. [47] is the Debye temperature: the *P6/mmm*-phase of $Nb_{0.75}Mo_{0.25}B_2$ superconductor exhibits strong nonadiabaticy, because the ratio

$$0.4 \ll \frac{T_\theta}{T_F} = 3.5 \pm 0.3, \tag{11}$$

is well above the typical range for the moderate level of nonadiabaticity ($0.025 \leq \frac{T_\theta}{T_F} \leq 0.4$) observed in the majority of unconventional superconductors, including iron-based, cuprates, and highly compressed hydrides [70] (Figures 4 and 5).

3.3. $P6_3/mmc$ WB_2 (P = 121.3 GPa)

Pei et al. [48] measured the $R(T)$ dataset for the WB_2 phase at $P = 121.3$ GPa, which was fitted to Equation (1) in Figure 7. The fit converged at $T_\theta = 440 \pm 1$ K and $R_{sat} \to \infty$. From the deduced T_θ, we found $\lambda_{e-ph} = 0.755$, for which we utilized the criterion of $\frac{R(T)}{R_{norm}(T)} = 0.18$, which is based on the presence of the inflection point in the $R(T, B, P = 121.3\ \text{GPa})$, as shown in Figure 2b,d of Ref. [48].

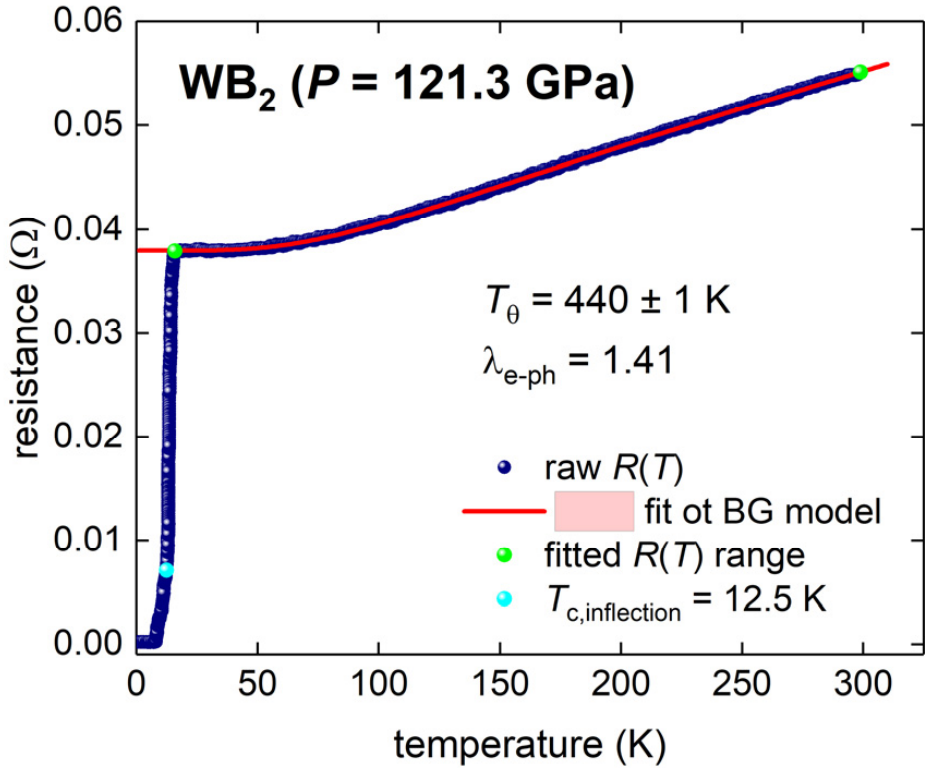

Figure 7. $R(T)$ data for highly compressed WB_2 (P = 121.3 GPa) and data fit to Equation (1) (raw data reported by Pei et al. [48]). Green balls indicate the bounds for which $R(T)$ data was used for the fit to Equation (1). Deduced $T_\theta = 440 \pm 1$ K, $T_{c,0.18} = 12.5$ K, $\lambda_{e-ph} = 0.755$, $R_{sat} = \infty$; fit quality is 0.9997. 95% confidence bands are shown by pink shadow areas.

By utilizing the resistance criterion of $\frac{R(T)}{R_{norm}(T)} = 0.18$ for $R(T, B)$ data reported in Figure 2d by Pei et al. [48], we deduced the $B_{c2}(T)$ dataset for WB_2 (P = 121.3 GPa). The fit of the $B_{c2}(T)$ dataset to the s-wave (Equations (6) and (7)) and d-wave models (Equations (8) and (9)) are shown in Figure 8.

The deduced parameters for s-wave (Figure 8a) contradict to each other, i.e., $\frac{2\Delta(0)}{k_B T_c} = 2.8 \pm 0.1$ (which is lower than the s-wave weak-coupling limit of $\frac{2\Delta(0)}{k_B T_c} = 3.53$ [66,67]), while the deduced $\frac{\Delta C}{\gamma T_c} = 1.6 \pm 0.4$ is slightly larger than the s-wave weak-coupling limit of $\frac{\Delta C}{\gamma T_c} = 1.43$. The fit quality is not high and has a coefficient of determination of 0.9019.

The fit to the d-wave gap symmetry model has a better quality (with a goodness of fit of 0.9986) (Figure 8b). The deduced parameters are $\xi(0) = 13.0$ nm, $\Delta(0) = 2.58 \pm 0.02$ meV, $\frac{2\Delta(0)}{k_B T_c} = 4.9 \pm 0.1$, $\frac{\Delta C}{\gamma T_c} = 1.19 \pm 0.07$. The parameters characterize the material as being a moderately strong coupled d-wave superconductor (considering that the weak coupling limits for d-wave superconductors [64–66] are $\frac{2 \cdot \Delta(0)}{k_B \cdot T_c} = 4.28$ and $\frac{\Delta C}{\gamma T_c} = 0.995$).

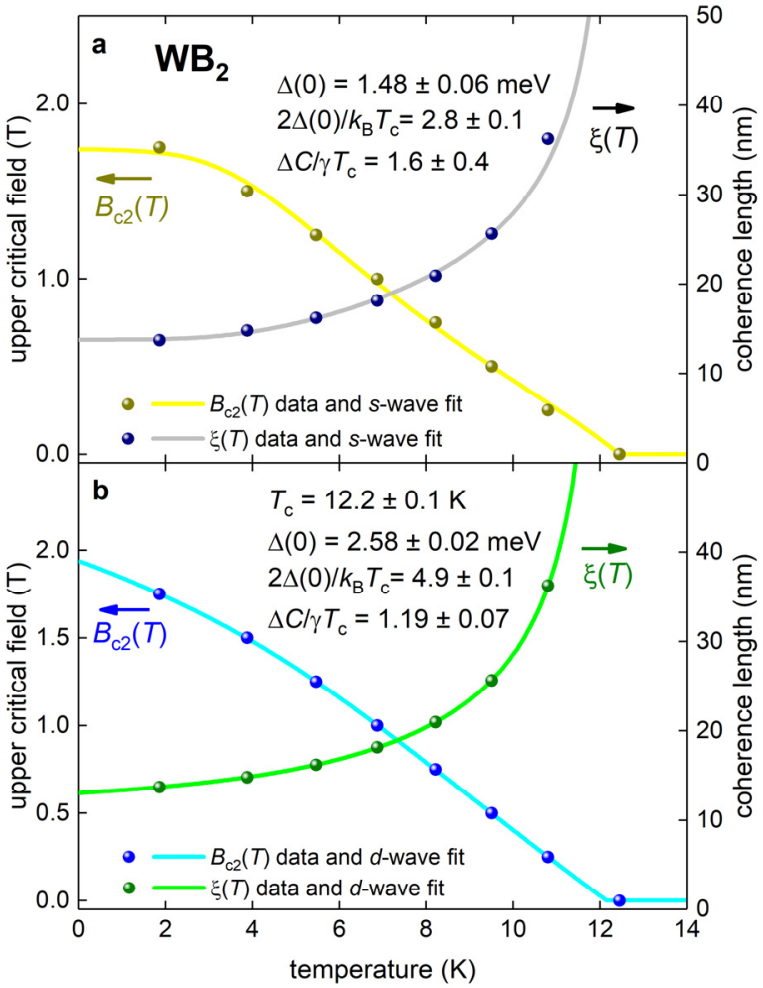

Figure 8. Temperature-dependent upper critical field, $B_{c2}(T)$, data (left Y-axes) (defined by $\frac{R(T)}{R_{norm}(T)} = 0.015$ criterion). Calculated by Equation (5): coherence length $\xi(T)$ (right Y-axes) for $P6_3/mmc$ WB_2 (P = 121.3 GPa) reported by Pei et al. [48] and data fits to *s*-wave (panel **a**) and *d*-wave (panel **b**) single-band models. Deduced parameters are (**a**) *s*-wave fit, T_c = 12.45 K (fixed), $\xi(0) = 13.8$ nm, $\Delta(0) = 1.48 \pm 0.06$ meV, $\Delta C/\gamma T_c = 1.6 \pm 0.4$, $\frac{2\Delta(0)}{k_B T_c} = 2.8 \pm 0.1$, the goodness of fit is 0.9019; (**b**) *d*-wave fit, $T_c = 12.2 \pm 0.2$ K, $\xi(0) = 13.0$ nm, $\Delta(0) = 2.58 \pm 0.02$ meV, $\Delta C/\gamma T_c = 1.19 \pm 0.07$, $\frac{2\Delta(0)}{k_B T_c} = 4.9 \pm 0.1$, the goodness of fit is 0.9986.

By substituting the deduced parameters in Equation (10), a Fermi temperature of $T_F = 1679 \pm 68$ K in WB_2 (P = 121.3 GPa) is calculated. The calculated T_F implies that this phase falls in the nearly conventional superconductors band in the Uemura plot (Figure 3), because this phase exhibits a reasonably low ratio of $\frac{T_c}{T_F} = 0.0077 \pm 0.0003$, while the typical range for unconventional superconductors is $0.01 \leq \frac{T_c}{T_F} \leq 0.05$.

This superconductor also exhibits a very moderate strength of nonadiabaticy, because the ratio:

$$0.025 < \frac{T_\theta}{T_F} = 0.26 \pm 0.01 < 0.4, \quad (12)$$

is typical for the majority of high-temperature superconductors, including iron-based, A15 alloys, Heusler alloys, Laves phase compounds, cuprates, and highly compressed hydrides [70] (Figures 4 and 5).

3.4. P6/mmm MgB_2

To demonstrate that the $B_{c2}(T)$ model (Equations (6)–(9) [61–63,74]) can be considered as an alternative model to extract primary superconducting parameters from $R(T, B)$

datasets (while the $B_{c2}(T)$ definition criterion is $\frac{R(T)}{R_{norm}(T)} \rightarrow 0$) in addition to the widely used Werthamer–Helfand–Hohenberg model [79,80], we showed $B_{c2}(T)$ data in Figure 9. The data were reported by Zehetmayer et al. [81] for single crystal MgB_2 and data fits to the single band *s*-wave (panel **a**, Equations (6) and (7)), the single band *d*-wave (panel **b**, Equations (8) and (9)), and the so-called two-band α-model [80] under the assumption of *s*-wave gap symmetry for both bands (panel **c**) [80,81]:

$$B_{c2,total}(T) = \alpha \times B_{c2,band1}(\xi_{total}(0), T) + (1 - \alpha) \times B_{c2,band2}(\xi_{total}(0), T), \quad (13)$$

To reduce the number of free-fitting parameters, we implemented the restriction [82]:

$$T_{c1} = T_{c2}, \quad (14)$$

$$\frac{\Delta C_1}{\gamma_1 T_{c1}} = \frac{\Delta C_2}{\gamma_2 T_{c2}}. \quad (15)$$

The deduced parameters for the single band *s*-wave model (Figure 9a) contradict each other, that is, $\frac{2\Delta(0)}{k_B T_c} = 3.3 \pm 0.1$ (which is lower than the *s*-wave weak-coupling limit). $\frac{\Delta C}{\gamma T_c} = 2.3 \pm 0.3$ is much larger than the *s*-wave weak-coupling limit. The deduced ratio of $\frac{2\Delta_m(0)}{k_B T_c} = 7.1 \pm 0.3$ for the *d*-wave model is nearly two times as large as the *d*-wave weak-coupling limit of $\frac{2\Delta_m(0)}{k_B T_c} = 4.28$, which is too large to be a realistic value.

However, the parameters deduced for the two-band α-model, $\alpha = 0.77 \pm 0.06$, $\frac{2\Delta_1(0)}{k_B T_c} = 4.1 \pm 0.3$, and $\frac{2\Delta_2(0)}{k_B T_c} = 1.7 \pm 0.2$, are in good agreement with the values deduced for MgB_2 by other techniques [83], in particular, by point contact spectroscopy [84].

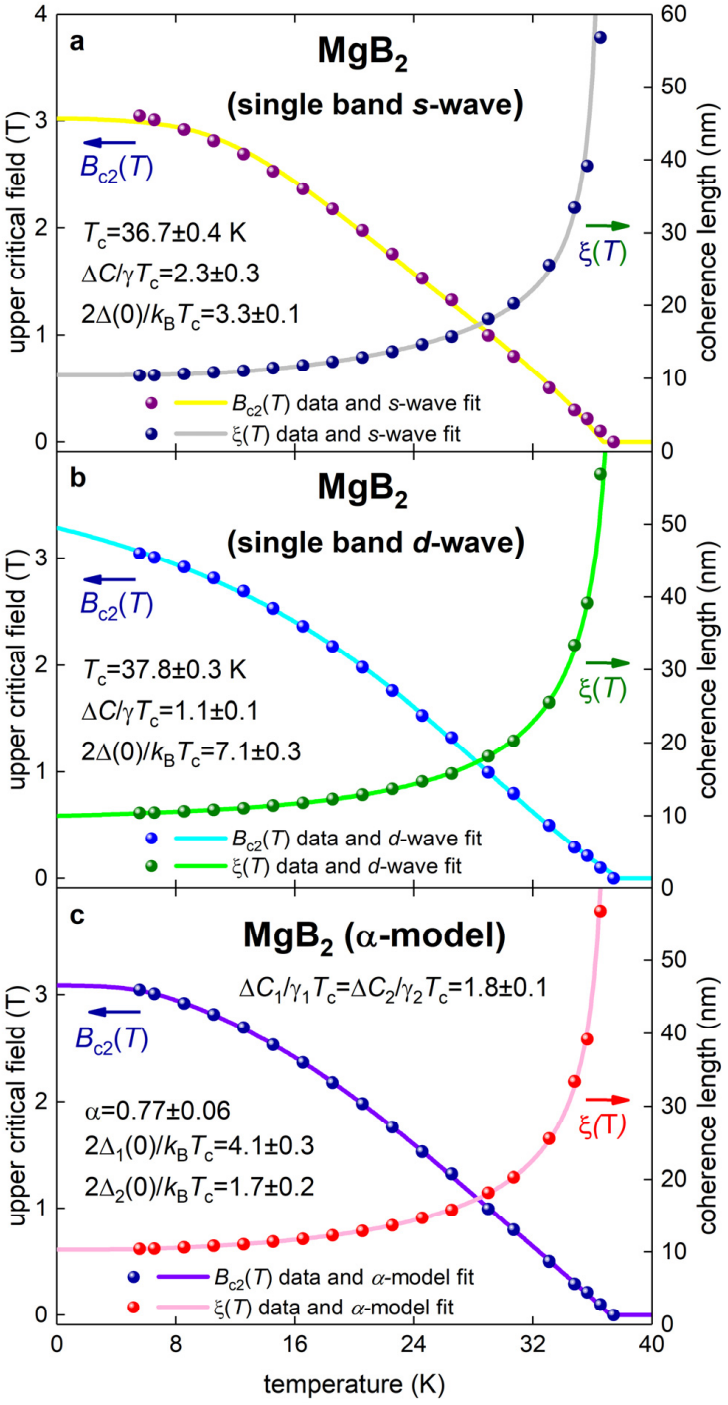

Figure 9. Temperature-dependent upper critical field, $B_{c2}(T)$, data (left Y-axes). Calculated by Equation (5): coherence length $\xi(T)$ (right Y-axes) for *P6/mmm* MgB_2 reported by Zehetmayer et al. [81] and data fits to single band *s*-wave (panel **a**, Equations (6) and (7)), single band *d*-wave (panel **b**, Equations (8) and (9)), and two-band *s*-wave [82,83] (panel **c**, Equations (6) and (7), Equations (13)–(15)) models. Deduced parameters are: (**a**) *s*-wave fit, $T_c = 36.7 \pm 0.4$ K, $\xi(0) = 10.4$ nm $\Delta(0) = 5.22 \pm 0.09$ meV, $\Delta C/\gamma T_c = 2.3 \pm 0.3$, $\frac{2\Delta(0)}{k_B T_c} = 3.3 \pm 0.1$, the goodness of fit is 0.9887; (**b**) *d*-wave fit, $T_c = 37.8 \pm 0.3$ K, $\xi(0) = 10.0$ nm, $\Delta_m(0) = 11.6 \pm 0.5$ meV, $\Delta C/\gamma T_c = 1.15 \pm 0.07$, $\frac{2\Delta_m(0)}{k_B T_c} = 7.1 \pm 0.3$, the goodness of fit is 0.9975. (**c**) two conditions where used: $T_{c1} = T_{c2} = 37.2 \pm 0.2$ K and $\frac{\Delta C_1}{\gamma_1 T_{c1}} = \frac{\Delta C_2}{\gamma_2 T_{c2}} = 1.8 \pm 0.1$, and other free-fitting parameters are: $\xi_{total}(0) = 10.3$ nm, $\alpha = 0.77 \pm 0.06$, $\Delta_1(0) = 6.5 \pm 0.4$ meV, $\frac{2\Delta_1(0)}{k_B T_c} = 4.1 \pm 0.3$, $\Delta_2(0) = 2.7 \pm 0.4$ meV, $\frac{2\Delta_2(0)}{k_B T_c} = 1.7 \pm 0.2$, the goodness of fit is 0.9984.

4. Discussion

In the consideration above, we calculated the electron–phonon coupling constant, λ_{e-ph}, with the assumption that diborides exhibit the Coulomb pseudopotential parameter, $\mu^* = 0.13$. The latter value is typical value for *s*-wave superconductors [67]. While our analysis of the upper critical field, $B_{c2}(T)$, showed that the materials exhibited *d*-wave gap symmetry, it is useful to show the variation in λ_{e-ph} calculated in the assumption of *d*-wave superconductivity. Santi et al. [85] reported that *d*-wave superconductors exhibit much lower μ^* values in comparison with *s*-wave superconductors. In Table 1, we listed calculated λ_{e-ph} values for all studied dibories (apart MgB_2) in accordance with Equations (2)–(4), with the assumption of $\mu^* = 0.00; 0.05; 0.10;$ and 0.13.

Table 1. Calculated the electron–phonon coupling constant, λ_{e-ph}, for assumed $\mu^* = 0.00; 0.05; 0.10;$ and 0.13 for studied diboride compounds α-MoB_2, $Nb_{0.75}Mo_{0.25}B_2$, and WB_2.

Compound	T_θ (K)	T_c (K)	Assumed μ^*	λ_{e-ph}
α-MoB_2 (109.7 GPa)	321	28.2	0.00	0.935
			0.05	1.10
			0.10	1.29
			0.13	1.41
$Nb_{1-x}MoxB_2$ (x = 0.25)	625	7.2	0.00	0.337
			0.05	0.422
			0.10	0.514
			0.13	0.573
WB_2 (121.3 GPa)	440	12.5	0.00	0.475
			0.05	0.575
			0.10	0.685
			0.13	0.755

The *P6/mmm*-phase of $Nb_{0.75}Mo_{0.25}B_2$ exhibits pronounced nonadiabaticity, $\frac{T_\theta}{T_F} = 3.5$. This value is well above an empirical border, $\frac{T_\theta}{T_F} \cong 0.4$. The majority of conventional and unconventional superconductors are located below this value (Figures 4 and 5). We can propose that the strength of the nonadiabaticity is a primary reason for the relatively low T_c in this material in comparison with other diboride counterparts. A good support for this hypothesis can be seen in Figure 5, where the T_c suppression within four dibories is linked to the increase in the strength of the nonadiabaticity. It can also be seen in Figure 5 that no materials simultaneously exhibit $T_c > 10$ K and $\frac{T_\theta}{T_F} > 0.4$.

Another explanation for the relatively low T_c in $Nb_{0.75}Mo_{0.25}B_2$ is the Abrikosov–Gor'kov [86], Anderson [87], and Openov [88,89] theory of dirty superconductors. The theory established that impurities with magnetic moments suppress the superconducting transition temperature, if the material exhibits *s*-wave superconductivity. However, magnetic impurities not affect the superconducting transition temperature in *d*-wave superconductors. From other hand, non-magnetic impurities cause the suppression of transition temperature in *d*-wave superconductors, and these impurities not affect the *s*-wave superconductors transition temperature.. Considering that the (Nb,Mo)-(0001) planes in *P6/mmm*-phase have chemical atomic disorder, because Hire et al. [47] did not report any evidence for the atomic ordering within Nb-Mo atoms in the (0001) planes, it appears that the T_c suppression in $Nb_{0.75}Mo_{0.25}B_2$ (and in all materials in the $Nb_{1-x}Mo_xB_2$ (x = 0.25; 0.50; 0.75 and 0.9) system) can be interpreted as T_c suppression in *d*-wave MoB_2 superconductors by nonmagnetic impurity—Nb/Mo atoms. However, we need to note that NbB_2 and MoB_2 are non-superconductors and these compounds exhibit different crystalline structures (*P6*/*mmm* and $R\bar{3}m$, respectively). Thus, the influence of the Nb/Mo atoms composition in (0001) planes on band structure and phonon spectra required more detailed experimental and first-principles calculation studies.

To consider the problem of the superconducting gap symmetry in diborides in a more general context, we should mention that there are several theoretical possibilities for the interplay between *s*- and *d*-wave symmetries for different compounds within the same group of superconductors, and even for the same compound at different condition. For instance, we can mention the infinite layer nickelates, where both gap symmetries were observed in experiment [90–92]. Wang et al. [93] reported the theoretical consideration that a very delicate boundary between a realization for one of two symmetries has been established.

Considering that all diborides considered here exhibit a layered structure with alternative atomic layers along the *c*-axis, one can expect a similarity between considered diborides and other anisotropic superconductors. For instance, in one of the seminal papers regarding cuprates (Uemura et al. [94]), the muon spin relaxation (μSR) data for Tl-based cuprates (showed in their Figure 1 [94]) can be interpreted exclusively as data supporting *s*-wave superconducting energy gap symmetry in cuprates. However, four years later, Uemura et al. [95] reported more extended μSR data for Tl-based cuprates, where temperature-dependent superfluid data for samples with low doping states can be still interpreted within *s*-wave symmetry, while low temperature data for overdoped samples are typical for *d*-wave linear dependence on temperature.

In addition, while our consideration is mainly focused on highly pressurized materials, we can mention another class of layered superconductors: iron-based superconductors. In these superconductors, the interplay between *s*- and *d*-wave gap symmetries was observed for the same compound in experiment. For instance, Guguchia et al. [96] reported that, at a pressure of several gigapascals, $Ba_{0.65}Rb_{0.35}Fe_2As_2$ (a two-band *s*-wave superconductor) exhibits a transition into a *d*-wave superconductor: " . . . hydrostatic pressure promotes the appearance of nodes in the superconducting gap . . . " [96].

Another purely theoretical possibility exists for a crossover between the electron–phonon and the electron–plasmon mediated pairing in layered superconductors. This possibility was recently proposed by in 't Veld et al. [97]. This is another possibility that shows how high-pressure (which, as a rule, changes the screening length in the compound) can induce the change in the pairing symmetry from *s*-wave (which is widely considered to be a consequence of the electron–phonon interaction) to nodal symmetry (which is widely accepted to be attributed to non-electron-phonon mediated pairing).

In overall, our analysis of experimental data on dibories—apart from MgB_2—showed that *d*-wave gap symmetry can explain experimental data with much better consistency. However, theoretical understanding of this result is still ongoing.

5. Conclusions

The field of experimental and theoretical studies of materials with strongly correlated charge carriers [5–44,46–49,57,59–61,74,98–116], including diborides [44,46–49,107,108], is experiencing a boom. In this work, we deduced the primary superconducting parameters of highly compressed diborides: the *P6/mmm* phases of MoB_2 and WB_2 and ambient pressure superconductors $Nd_{0.75}Mo_{0.25}B_2$. It was shown that these the compounds exhibit *d*-wave superconducting gap symmetry. We proposed that the suppression of the superconducting transition temperature (down to $T_c = 8$ K) in $Nb_{0.75}Mo_{0.25}B_2$ can be either related to strong nonadiabaticity in this phase (which exhibits the ratio $\frac{T_\theta}{T_F} = 3.5$) or to the effect of the T_c suppression in *d*-wave MoB_2 superconductors by nonmagnetic impurities (Nb/Mo atoms).

Funding: This research was funded by the Ministry of Science and Higher Education of the Russian Federation, grant number No. AAAA-A18-118020190104-3 (theme "Pressure"). The research funding from the Ministry of Science and Higher Education of the Russian Federation (Ural Federal University Program of Development within the Priority-2030 Program) is gratefully acknowledged.

Institutional Review Board Statement: Not applicable.

Informed Consent Statement: Not applicable.

Data Availability Statement: Not applicable.

Acknowledgments: The author thanks Svetoslav A. Kuzmichev (Lomonosov Moscow State University) for the discussion about dirty *s*- and *d*-wave superconductors.

Conflicts of Interest: The author declares no conflict of interest. The funders had no role in the design of the study; in the collection, analyses, or interpretation of data; in the writing of the manuscript; or in the decision to publish the results.

References

1. Satterthwaite, C.B.; Toepke, I.L. Superconductivity of hydrides and deuterides of thorium. *Phys. Rev. Lett.* **1970**, *25*, 741–743. [CrossRef]
2. Cooper, A.S.; Corenzwit, E.; Longinotti, L.D.; Matthias, B.T.; Zachariasen, W.H. Superconductivity: The transition temperature peak below four electrons per atom. *Proc. Natl. Acad. Sci. USA* **1970**, *67*, 313–319. [CrossRef]
3. Fisk, Z. Superconducting borides. *AIP Conf. Proc.* **1991**, *231*, 155–164.
4. Nagamatsu, J.; Nakagawa, N.; Muranaka, T.; Zenitani, Y.; Akimitsu, J. Superconductivity at 39 K in magnesium diboride. *Nature* **2001**, *410*, 63–64. [CrossRef]
5. Drozdov, A.P.; Eremets, M.I.; Troyan, I.A.; Ksenofontov, V.; Shylin, S.I. Conventional superconductivity at 203 kelvin at high pressures in the sulfur hydride system. *Nature* **2015**, *525*, 73–76. [CrossRef]
6. Drozdov, A.P.; Kong, P.P.; Minkov, V.S.; Besedin, S.P.; Kuzovnikov, M.A.; Mozaffari, S.; Balicas, L.; Balakirev, F.F.; Graf, D.E.; Prakapenka, V.B.; et al. Superconductivity at 250 K in lanthanum hydride under high pressures. *Nature* **2019**, *569*, 528–531. [CrossRef] [PubMed]
7. Somayazulu, M.; Ahart, M.; Mishra, A.K.; Geballe, Z.M.; Baldini, M.; Meng, Y.; Struzhkin, V.V.; Hemley, R.J. Evidence for superconductivity above 260 K in lanthanum superhydride at megabar pressures. *Phys. Rev. Lett.* **2019**, *122*, 027001. [CrossRef] [PubMed]
8. Semenok, D.V.; Kvashnin, A.G.; Ivanova, A.G.; Svitlyk, V.; Fominski, V.Y.; Sadakov, A.V.; Sobolevskiy, O.A.; Pudalov, V.M.; Troyan, I.A.; Oganov, A.R. Superconductivity at 161 K in thorium hydride ThH_{10}: Synthesis and properties. *Mater. Today* **2020**, *33*, 36–44. [CrossRef]
9. Troyan, I.A.; Semenok, D.V.; Kvashnin, A.G.; Sadakov, A.V.; Sobolevskiy, O.A.; Pudalov, V.M.; Ivanova, A.G.; Prakapenka, V.B.; Greenberg, E.; Gavriliuk, A.G.; et al. Anomalous high-temperature superconductivity in YH_6. *Adv. Mater.* **2021**, *33*, 2006832. [CrossRef]
10. Kong, P.; Minkov, V.S.; Kuzovnikov, M.A.; Drozdov, A.P.; Besedin, S.P.; Mozaffari, S.; Balicas, L.; Balakirev, F.F.; Prakapenka, V.B.; Chariton, S.; et al. Superconductivity up to 243 K in yttrium hydrides under high pressure. *Nat. Commun.* **2021**, *12*, 5075. [CrossRef] [PubMed]
11. Semenok, D.V.; Troyan, I.A.; Ivanova, A.G.; Kvashnin, A.G.; Kruglov, I.A.; Hanfland, M.; Sadakov, A.V.; Sobolevskiy, O.A.; Pervakov, K.S.; Lyubutin, I.S.; et al. Superconductivity at 253 K in lanthanum–yttrium ternary hydrides. *Mater. Today* **2021**, *48*, 18–28. [CrossRef]
12. Mozaffari, S.; Sun, D.; Minkov, V.S.; Drozdov, A.P.; Knyazev, D.; Betts, J.B.; Einaga, M.; Shimizu, K.; Eremets, M.I.; Balicas, L. Superconducting phase-diagram of H_3S under high magnetic fields. *Nat. Commun.* **2019**, *10*, 2522. [CrossRef] [PubMed]
13. Sun, D.; Minkov, V.S.; Mozaffari, S.; Sun, Y.; Ma, Y.; Chariton, S.; Prakapenka, V.B.; Eremets, M.I.; Balicas, L.; Balakirev, F.F. High-temperature superconductivity on the verge of a structural instability in lanthanum superhydride. *Nat. Commun.* **2021**, *12*, 6863. [CrossRef] [PubMed]
14. Chen, W.; Semenok, D.V.; Kvashnin, A.G.; Huang, X.; Kruglov, I.A.; Galasso, M.; Song, H.; Duan, D.; Goncharov, A.F.; Prakapenka, V.B.; et al. Synthesis of molecular metallic barium superhydride: Pseudocubic BaH_{12}. *Nat. Commun.* **2021**, *12*, 273. [CrossRef]
15. Bi, J.; Nakamoto, Y.; Zhang, P.; Shimizu, K.; Zou, B.; Liu, H.; Zhou, M.; Liu, G.; Wang, H.; Ma, Y. Giant enhancement of superconducting critical temperature in substitutional alloy $(La,Ce)H_9$. *Nat. Commun.* **2022**, *13*, 5952. [CrossRef] [PubMed]
16. Wang, Y.; Wang, K.; Sun, Y.; Ma, L.; Wang, Y.; Zou, B.; Liu, G.; Zhou, M.; Wang, H. Synthesis and superconductivity in yttrium superhydrides under high pressure. *Chinese Physics B* **2022**, *31*, 106201. [CrossRef]
17. Ma, L.; Wang, K.; Xie, Y.; Yang, X.; Wang, Y.; Zhou, M.; Liu, H.; Yu, X.; Zhao, Y.; Wang, H.; et al. High-temperature superconducting phase in clathrate calcium hydride CaH_6 up to 215 K at a pressure of 172 GPa. *Phys. Rev. Lett.* **2022**, *128*, 167001. [CrossRef]
18. Zhou, D.; Semenok, D.V.; Duan, D.; Xie, H.; Chen, W.; Huang, X.; Li, X.; Liu, B.; Oganov, A.R.; Cui, T. Superconducting praseodymium superhydrides. *Sci. Adv.* **2020**, *6*, eaax6849. [CrossRef]
19. Hong, F.; Shan, P.F.; Yang, L.X.; Yue, B.B.; Yang, P.T.; Liua, Z.Y.; Sun, J.P.; Dai, J.H.; Yu, H.; Yin, Y.Y.; et al. Possible superconductivity at ∼70 K in tin hydride SnH_x under high pressure. *Mater. Today Phys.* **2022**, *22*, 100596. [CrossRef]
20. Chen, W.; Semenok, D.V.; Huang, X.; Shu, H.; Li, X.; Duan, D.; Cui, T.; Oganov, A.R. High-temperature superconducting phases in cerium superhydride with a T_c up to 115 K below a pressure of 1 Megabar. *Phys. Rev. Lett.* **2021**, *127*, 117001. [CrossRef]
21. Osmond, I.; Moulding, O.; Cross, S.; Muramatsu, T.; Brooks, A.; Lord, O.; Fedotenko, T.; Buhot, J.; Friedemann, S. Clean-limit superconductivity in *Im3m* H_3S synthesized from sulfur and hydrogen donor ammonia borane. *Phys. Rev. B* **2022**, *105*, L220502. [CrossRef]

22. Semenok, D.V.; Troyan, I.A.; Sadakov, A.V.; Zhou, D.; Galasso, M.; Kvashnin, A.G.; Ivanova, A.G.; Kruglov, I.A.; Bykov, A.A.; Terent'ev, K.Y.; et al. Effect of magnetic impurities on superconductivity in LaH_{10}. *Adv. Mater.* **2022**, *34*, 2204038. [CrossRef] [PubMed]
23. Li, Z.; He, X.; Zhang, C.; Wang, X.; Zhang, S.; Jia, Y.; Feng, S.; Lu, K.; Zhao, J.; Zhang, J.; et al. Superconductivity above 200 K discovered in superhydrides of calcium. *Nat. Commun.* **2022**, *13*, 2863. [CrossRef] [PubMed]
24. Minkov, V.S.; Bud'ko, S.L.; Balakirev, F.F.; Prakapenka, V.B.; Chariton, S.; Husband, R.J.; Liermann, H.P.; Eremets, M.I. Magnetic field screening in hydrogen-rich high-temperature superconductors. *Nat. Commun.* **2022**, *13*, 3194. [CrossRef]
25. Minkov, V.S.; Prakapenka, V.B.; Greenberg, E.; Eremets, M.I. A boosted critical temperature of 166 K in superconducting D_3S synthesized from elemental sulfur and hydrogen. *Angew. Chem. Int. Ed.* **2020**, *59*, 18970–18974. [CrossRef]
26. Liu, Z.Y.; Dong, Q.X.; Yang, P.T.; Shan, P.F.; Wang, B.S.; Sun, J.P.; Dun, Z.L.; Uwatoko, Y.; Chen, G.F.; Dong, X.L.; et al. Pressure-induced superconductivity up to 9 K in the quasi-one-dimensional KMn_6Bi_5. *Phys. Rev. Lett.* **2022**, *128*, 187001. [CrossRef]
27. Minkov, V.S.; Ksenofontov, V.; Budko, S.L.; Talantsev, E.F.; Eremets, M.I. Trapped magnetic flux in hydrogen-rich high-temperature superconductors. *arXiv* **2022**, arXiv:2206.14108. [CrossRef]
28. He, X.; Zhang, C.L.; Li, Z.W.; Zhang, S.J.; Min, B.S.; Zhang, J.; Lu, K.; Zhao, J.F.; Shi, L.C.; Peng, Y.; et al. Superconductivity observed in tantalum polyhydride at high pressure. *arXiv* **2022**, arXiv:2212.13739. [CrossRef]
29. Wang, H.; Tse, J.S.; Tanaka, K.; Iitaka, T.; Ma, Y. Superconductive sodalite-like clathrate calcium hydride at high pressures. *Proc. Natl. Acad. Sci. USA* **2012**, *109*, 6463–6466. [CrossRef]
30. Lyakhov, A.O.; Oganov, A.R.; Stokes, H.T.; Zhu, Q. New developments in evolutionary structure prediction algorithm USPEX. *Comput. Phys. Commun.* **2013**, *184*, 1172–1182. [CrossRef]
31. Li, Y.; Hao, J.; Liu, H.; Li, Y.; Ma, Y. The metallization and superconductivity of dense hydrogen sulphide. *J. Chem. Phys.* **2014**, *140*, 174712. [CrossRef]
32. Duan, D.; Liu, Y.; Tian, F.; Li, D.; Huang, X.; Zhao, Z.; Yu, H.; Liu, B.; Tian, W.; Cui, T. Pressure-induced metallization of dense $(H_2S)_2H_2$ with high-T_c superconductivity. *Sci. Rep.* **2014**, *4*, 6968. [CrossRef] [PubMed]
33. Heil, C.; di Cataldo, S.; Bachelet, G.B.; Boeri, L. Superconductivity in sodalite-like yttrium hydride clathrates. *Phys. Rev. B* **2019**, *99*, 220502. [CrossRef]
34. Flores-Livas, J.A.; Boeri, L.; Sanna, A.; Profeta, G.; Arita, R.; Eremets, M. A perspective on conventional high-temperature superconductors at high pressure: Methods and materials. *Phys. Rep.* **2020**, *856*, 1–78. [CrossRef]
35. Struzhkin, V.; Li, B.; Ji, C.; Chen, X.-J.; Prakapenka, V.; Greenberg, E.; Troyan, I.; Gavriliuk, A.; Mao, H.-k. Superconductivity in La and Y hydrides: Remaining questions to experiment and theory. *Matter Radiat. Extrem.* **2020**, *5*, 028201. [CrossRef]
36. Errea, I.; Belli, F.; Monacelli, L.; Sanna, A.; Koretsune, T.; Tadano, T.; Bianco, R.; Calandra, M.; Arita, R.; Mauri, F.; et al. Quantum crystal structure in the 250-kelvin superconducting lanthanum hydride. *Nature* **2020**, *578*, 66–69. [CrossRef] [PubMed]
37. Gregoryanz, E.; Ji, C.; Dalladay-Simpson, P.; Li, B.; Howie, R.T.; Mao, H.-K. Everything you always wanted to know about metallic hydrogen but were afraid to ask. *Matter Radiat. Extrem.* **2020**, *5*, 038101. [CrossRef]
38. Boeri, L.; Hennig, R.; Hirschfeld, P.; Profeta, G.; Sanna, A.; Zurek, E.; Pickett, W.E.; Amsler, M.; Dias, R.; Eremets, M.I.; et al. The 2021 room-temperature superconductivity roadmap. *J. Phys. Condens. Matter* **2021**, *34*, 183002.
39. Shao, M.; Chen, W.; Zhang, K.; Huang, X.; Cui, T. High-pressure synthesis of superconducting clathratelike YH_4. *Phys. Rev. B* **2021**, *104*, 174509. [CrossRef]
40. Amiel, Y.; Kafle, G.P.; Komleva, E.V.; Greenberg, E.; Ponosov, Y.S.; Chariton, S.; Lavina, B.; Zhang, D.; Palevski, A.; Ushakov, A.V.; et al. Silvanite $AuAgTe_4$: A rare case of gold superconducting material. *arXiv* **2023**, arXiv:2301.08033. [CrossRef]
41. Mao, H.-K. Hydrogen and related matter in the pressure dimension. *Matter Radiat. Extrem.* **2022**, *7*, 063001. [CrossRef]
42. Zhang, Z.; Cui, T.; Hutcheon, M.J.; Shipley, A.M.; Song, H.; Du, M.; Kresin, V.Z.; Duan, D.; Pickard, C.J.; Yao, Y. Design principles for high-temperature superconductors with a hydrogen-based alloy backbone at moderate pressure. *Phys. Rev. Lett.* **2022**, *128*, 047001. [CrossRef] [PubMed]
43. Du, M.; Song, H.; Zhang, Z.; Duan, D.; Cui, T. Room-temperature superconductivity in Yb/Lu substituted clathrate hexahydrides under moderate pressure. *Research* **2022**, *2022*, 9784309. [CrossRef] [PubMed]
44. Pei, C.; Zhang, J.; Wang, Q.; Zhao, Y.; Gao, L.; Gong, C.; Tian, S.; Luo, R.; Li, M.; Yang, W.; et al. Pressure-induced superconductivity at 32 K in MoB_2. *Natl. Sci. Rev.* **2023**, *10*, nwad034, *in press*. [CrossRef]
45. Zhuang, C.G.; Meng, S.; Zhang, C.Y.; Feng, Q.R.; Gan, Z.Z.; Yang, H.; Jia, Y.; Wen, H.H.; Xi, X.X. Ultrahigh current-carrying capability in clean MgB_2 films. *J. Appl. Phys.* **2008**, *104*, 013924. [CrossRef]
46. Quan, Y.; Lee, K.-W.; Pickett, W.E. MoB_2 under pressure: Superconducting Mo enhanced by boron. *Phys. Rev. B* **2021**, *104*, 224504. [CrossRef]
47. Hire, A.C.; Sinha, S.; Lim, J.; Kim, J.S.; Dee, P.M.; Fanfarillo, L.; Hamlin, J.J.; Hennig, R.G.; Hirschfeld, P.J.; Stewart, G.R. High critical field superconductivity at ambient pressure in MoB_2 stabilized in the *P6/mmm* structure via Nb substitution. *Phys. Rev. B* **2022**, *106*, 174515. [CrossRef]
48. Pei, C.; Zhang, J.; Gong, C.; Wang, Q.; Gao, L.; Zhao, Y.; Tian, S.; Cao, W.; Li, C.; Lu, Z.-Y.; et al. Distinct superconducting behaviours of pressurized WB_2 and ReB_2 with different local B layers. *Sci. China-Phys. Mech. Astron.* **2022**, *65*, 287412. [CrossRef]
49. Lim, J.; Hire, A.C.; Quan, Y.; Kim, J.S.; Xie, S.R.; Sinha, S.; Kumar, R.S.; Popov, D.; Park, C.; Hemley, R.J.; et al. Creating superconductivity in WB_2 through pressure-induced metastable planar defects. *Nat. Commun.* **2022**, *13*, 7901. [CrossRef]

50. Zandbergen, H.W.; Gronsky, R.; Wang, K.; Thomas, G. Structure of $(CuO)_2$ double layers in superconducting $YBa_2Cu_3O_7$. *Nature* **1988**, *331*, 596–599. [CrossRef]
51. Specht, E.D.; Goyal, A.; Li, J.; Martin, P.M.; Li, X.; Rupich, M.W. Stacking faults in $YBa_2Cu_3O_{7-x}$: Measurement using X-ray diffraction and effects on critical current. *Appl. Phys. Lett.* **2006**, *89*, 162510. [CrossRef]
52. Talantsev, E.F.; Strickland, N.M.; Wimbush, S.C.; Storey, J.G.; Tallon, J.L.; Long, N.J. Hole doping dependence of critical current density in $YBa_2Cu_3O_{7-\delta}$ conductors. *Appl. Phys. Lett.* **2014**, *104*, 242601. [CrossRef]
53. Bloch, F. Zum elektrischen Widerstandsgesetz bei tiefen Temperaturen. *Z. Phys.* **1930**, *59*, 208–214. [CrossRef]
54. Grüneisen, E. Die abhängigkeit des elektrischen widerstandes reiner metalle von der temperatur. *Ann. Phys.* **1933**, *408*, 530–540. [CrossRef]
55. Fisk, Z.; Webb, G.W. Saturation of the high-temperature normal-state electrical resistivity of superconductors. *Phys. Rev. Lett.* **1976**, *36*, 1084–1086. [CrossRef]
56. Wiesmann, H.; Gurvitch, M.; Lutz, H.; Ghosh, A.; Schwarz, B.; Strongin, M.; Allen, P.B.; Halley, J.W. Simple model for characterizing the electrical resistivity in A-15 superconductors. *Phys. Rev. Lett.* **1977**, *38*, 782–785. [CrossRef]
57. Matsumoto, R.; Song, P.; Adachi, S.; Saito, Y.; Hara, H.; Yamashita, A.; Nakamura, K.; Yamamoto, S.; Tanaka, H.; Irifune, T.; et al. Pressure-induced superconductivity in tin sulfide. *Phys. Rev. B* **2019**, *99*, 184502. [CrossRef]
58. Kudo, K.; Hiiragi, H.; Honda, T.; Fujimura, K.; Idei, H.; Nohara, M. Superconductivity in Mg_2Ir_3Si: A fully ordered Laves phase. *J. Phys. Soc. Jpn.* **2020**, *89*, 013701. [CrossRef]
59. Talantsev, E.F. Advanced McMillan's equation and its application for the analysis of highly-compressed superconductors. *Supercond. Sci. Technol.* **2020**, *33*, 094009. [CrossRef]
60. Talantsev, E.F. The electron–phonon coupling constant and the Debye temperature in polyhydrides of thorium, hexadeuteride of yttrium, and metallic hydrogen phase III. *J. Appl. Phys.* **2021**, *130*, 195901. [CrossRef]
61. Talantsev, E.F. Classifying superconductivity in compressed H_3S. *Mod. Phys. Lett. B* **2019**, *33*, 1950195. [CrossRef]
62. Talantsev, E.F. In-plane p-wave coherence length in iron-based superconductors. *Results Phys.* **2020**, *18*, 103339. [CrossRef]
63. Talantsev, E.F.; Mataira, R.C.; Crump, W.P. Classifying superconductivity in Moiré graphene superlattices. *Sci. Rep.* **2020**, *10*, 212. [CrossRef]
64. Gross, F.; Chandrasekhar, B.S.; Einzel, D.; Andres, K.; Hirschfeld, P.J.; Ott, H.R.; Beuers, J.; Fisk, Z.; Smith, J.L. Anomalous temperature dependence of the magnetic field penetration depth in superconducting UBe_{13}. *Z. Phys. B* **1986**, *64*, 175–188. [CrossRef]
65. Gross-Alltag, F.; Chandrasekhar, B.S.; Einzel, D.; Hirschfeld, P.J.; Andres, K. London field penetration in heavy fermion superconductors. *Z. Phys. B* **1991**, *82*, 243–255. [CrossRef]
66. Bardeen, J.; Cooper, L.N.; Schrieffer, J.R. Theory of superconductivity. *Phys. Rev.* **1957**, *108*, 1175–1204. [CrossRef]
67. Carbotte, J.P. Properties of boson-exchange superconductors. *Rev. Mod. Phys.* **1990**, *62*, 1027–1157. [CrossRef]
68. Talantsev, E.F.; Crump, W.P.; Tallon, J.L. Thermodynamic parameters of single- or multi-band superconductors derived from self-field critical currents. *Ann. Phys.* **2017**, *529*, 1700197. [CrossRef]
69. Pietronero, L.; Boeri, L.; Cappelluti, E.; Ortenzi, L. Conventional/unconventional superconductivity in high-pressure hydrides and beyond: Insights from theory and perspectives. *Quantum Stud. Math. Found.* **2018**, *5*, 5–21. [CrossRef]
70. Talantsev, E.F. Quantifying nonadiabaticity in major families of superconductors. *Nanomaterials* **2023**, *13*, 71. [CrossRef]
71. Talantsev, E.F.; Tallon, J.L. Universal self-field critical current for thin-film superconductors. *Nat. Commun.* **2015**, *6*, 7820. [CrossRef] [PubMed]
72. Cappelluti, E.; Ciuchi, S.; Grimaldi, C.; Pietronero, L.; Strässler, S. High T_c superconductivity in MgB_2 by nonadiabatic pairing. *Phys. Rev. Lett.* **2002**, *88*, 117003. [CrossRef] [PubMed]
73. Papagelis, K.; Arvanitidis, J.; Margiolaki, I.; Brigatti, K.; Prassides, K.; Schenck, A.; Lappas, A.; Amato, A.; Iwasa, Y.; Takenobu, T. μSR studies of superconducting $MgB_{1.96}C_{0.04}$. *Phys. B* **2003**, *326*, 346–349. [CrossRef]
74. Talantsev, E.F. Electron–phonon coupling constant and BCS ratios in LaH_{10-y} doped with magnetic rare-earth element. *Supercond. Sci. Technol.* **2022**, *35*, 095008. [CrossRef]
75. Patra, C.; Agarwal, T.; Chaudhari, R.R.; Singh, R.P. Two-dimensional multigap superconductivity in bulk 2H-TaSeS. *Phys. Rev. B* **2022**, *106*, 134515. [CrossRef]
76. Park, S.; Kim, S.Y.; Kim, H.K.; Kim, M.J.; Kim, T.; Kim, H.; Choi, G.S.; Won, C.J.; Kim, S.; Kim, K.; et al. Superconductivity emerging from a stripe charge order in $IrTe_2$ nanoflakes. *Nat. Commun.* **2021**, *12*, 3157. [CrossRef]
77. Szczesniak, D.; Kaczmarek, A.Z.; Drzazga-Szczesniak, E.A.; Szczesniak, R. Phonon-mediated superconductivity in bismuthates by nonadiabatic pairing. *Phys. Rev. B* **2021**, *104*, 094501. [CrossRef]
78. Szczesniak, D.; Szczesniak, R. Signatures of nonadiabatic superconductivity in lithium-decorated graphene. *Phys. Rev. B* **2019**, *99*, 224512. [CrossRef]
79. Helfand, E.; Werthamer, N.R. Temperature and purity dependence of the superconducting critical field, H_{c2}. II. *Phys. Rev.* **1966**, *147*, 288–294. [CrossRef]
80. Werthamer, N.R.; Helfand, E.; Hohenberg, P.C. Temperature and purity dependence of the superconducting critical field, H_{c2}. III. Electron spin and spin-orbit effects. *Phys. Rev.* **1966**, *147*, 295–302. [CrossRef]
81. Zehetmayer, M.; Eisterer, M.; Jun, J.; Kazakov, S.M.; Karpinski, J.; Wisniewski, A.; Weber, H.W. Mixed-state properties of superconducting MgB_2 single crystals. *Phys. Rev. B* **2002**, *66*, 052505. [CrossRef]

82. Bouquet, F.; Wang, Y.; Fisher, R.A.; Hinks, D.G.; Jorgensen, J.D.; Junod, A.; Phillips, N.E. Phenomenological two-gap model for the specific heat of MgB_2. *Europhys. Lett.* **2001**, *56*, 856. [CrossRef]
83. Talantsev, E.F.; Crump, W.P.; Island, J.O.; Xing, Y.; Sun, Y.; Wang, J.; Tallon, J.L. On the origin of critical temperature enhancement in atomically thin superconductors. *2D Mater.* **2017**, *4*, 025072. [CrossRef]
84. Szabó, P.; Samuely, P.; Kačmarčík, J.; Klein, T.; Marcus, J.; Fruchart, D.; Miraglia, S.; Marcenat, C.; Jansen, A.G.M. Evidence for two superconducting energy gaps in MgB_2 by point-contact spectroscopy. *Phys. Rev. Lett.* **2001**, *87*, 137005. [CrossRef]
85. Santi, G.; Jarlborg, T.; Peter, M.; Weger, M. Existence of both s and *d*-wave solutions of Eliashberg equations. *J. Supercond.* **1995**, *8*, 405–408. [CrossRef]
86. Gor'kov, L.P. *Superconductivity: Conventional and Unconventional Superconductors*; Bennemann, K.H., Ketterson, J.B., Eds.; Springer: Berlin/Heidelberg, Germany, 2008; pp. 201–224.
87. Anderson, P.W. Theory of dirty superconductors. *J. Phys. Chem. Solids* **1959**, *11*, 26–30. [CrossRef]
88. Openov, L.A. Critical temperature of an anisotropic superconductor containing both nonmagnetic and magnetic impurities. *Phys. Rev. B* **1998**, *58*, 9468–9478. [CrossRef]
89. Openov, L.A. Effect of nonmagnetic and magnetic impurities on the specific heat jump in anisotropic superconductors. *Phys. Rev. B* **2004**, *69*, 224516. [CrossRef]
90. Gu, Q.; Li, Y.; Wan, S.; Li, H.; Guo, W.; Yang, H.; Li, Q.; Zhu, X.; Pan, X.; Nie, Y.; et al. Single particle tunnelling spectrum of superconducting $Nd_{1-x}Sr_xNiO_2$ thin films. *Nat. Commun.* **2020**, *11*, 6027. [CrossRef]
91. Chow, L.E.; Sudheesh, S.K.; Nandi, P.; Zeng, S.W.; Zhang, Z.T.; Du, X.M.; Lim, Z.S.; Chia, E.E.M.; Ariando, A. Pairing symmetry in infinite-layer nickelate superconductor. *arXiv* **2022**, arXiv:2201.10038. [CrossRef]
92. Harvey, S.P.; Wang, B.Y.; Fowlie, J.; Osada, M.; Lee, K.; Lee, Y.; Li, D.; Hwang, H.Y. Evidence for nodal superconductivity in infinite-layer nickelates. *arXiv* **2022**, arXiv:2201.12971. [CrossRef]
93. Wang, Z.; Zhang, G.-M.; Yang, Y.-f.; Zhang, F.-C. Distinct pairing symmetries of superconductivity in infinite-layer nickelates. *Phys. Rev. B* **2020**, *102*, 220501. [CrossRef]
94. Uemura, Y.J.; Luke, G.M.; Sternlieb, B.J.; Brewer, J.H.; Carolan, J.F.; Hardy, W.N.; Kadono, R.; Kempton, J.R.; Kiefl, R.F.; Kreitzman, S.R. Universal correlations between T_c and $\frac{n_s}{m_*}$ (carrier density over effective mass) in high-T_c cuprate. *Phys. Rev. Lett.* **1989**, *62*, 2317–2320. [CrossRef]
95. Uemura, Y.J.; Keren, A.; Le, L.P.; Luke, G.M.; Wu, W.D.; Kubo, Y.; Manako, T.; Shimakawa, Y.; Subramanian, M.; Cobb, J.L.; et al. Magnetic-field penetration depth in $Tl_2Ba_2CuO_{6+\delta}$ in the overdoped regime. *Nature* **1993**, *364*, 605–607. [CrossRef]
96. Guguchia, Z.; Amato, A.; Kang, J.; Luetkens, H.; Biswas, P.K.; Prando, G.; von Rohr, F.; Bukowski, Z.; Shengelaya, A.; Keller, H.; et al. Direct evidence for a pressure-induced nodal superconducting gap in the $Ba_{0.65}Rb_{0.35}Fe_2As_2$ superconductor. *Nat. Commun.* **2015**, *6*, 8863. [CrossRef] [PubMed]
97. in 't Veld, Y.; Katsnelson, M.I.; Millis, A.J.; Rösner, M. Screening induced crossover between phonon- and plasmon-mediated pairing in layered superconductors. *arXiv* **2023**, arXiv:2303.06220. [CrossRef]
98. Talantsev, E.F. Classifying hydrogen-rich superconductors. *Mater. Res. Express* **2019**, *6*, 106002. [CrossRef]
99. Jorba, P.; Regnat, A.; Tong, A.; Seifert, M.; Bauer, A.; Schulz, M.; Franz, C.; Schneidewind, A.; Kunkemöller, S.; Jenni, K.; et al. High-pressure studies of correlated electron systems. *Phys. Status Solidi B* **2022**, *259*, 2100623. [CrossRef]
100. Ruangrungrote, S.; Chanpoom, T.; Thaninworapak, R.; Udomsamuthirun, P. Investigation of the gap-to-T_c ratio of LaH_{10} and LaD_{10} superconductors. *Int. J. Mod. Phys. B* **2023**, 37, *in press*. [CrossRef]
101. Chanilkul, G.; Changjan, A.; Nilkamjon, T.; Udomsamuthirun, P. External pressure effects on superfluid density of isotropic *s*-wave superconductors. *J. Phys. Conf. Ser.* **2023**, *2431*, 012043. [CrossRef]
102. Talantsev, E.F. Universal Fermi velocity in highly compressed hydride superconductors. *Matter Radiat. Extrem.* **2022**, *7*, 058403. [CrossRef]
103. Malik, G.P.; Varma, V.S. On the generalized BCS equations incorporating chemical potential for the T_c and the calculation of the coherence length of some elements and compressed H_3S. *J. Low Temp. Phys.* **2023**, *in press*. [CrossRef]
104. van de Bund, S.; Ackland, G.J. Competition between superconductivity and molecularization in quantum nuclear behavior of Lanthanum Hydride. *arXiv* **2023**, arXiv:2303.01441. [CrossRef]
105. Feng, X.Y.; Zhao, Z.; Luo, J.; Yang, J.; Fang, A.F.; Yang, H.T.; Gao, H.J.; Zhou, R.; Zheng, G.-Q. Commensurate-to-incommensurate transition of charge-density-wave order and a possible quantum critical point in pressurized kagome metal CsV_3Sb_5. *arXiv* **2023**, arXiv:2303.01225. [CrossRef]
106. He, X.; Zhang, C.; Li, Z.; Liua, C.; Feng, S.; Zhao, J.; Lu, K.; Bin, B.; Zhang, S.; Peng, Y.; et al. Superconductivity above 30 K achieved in dense scandium. *arXiv* **2023**, arXiv:2303.01062. [CrossRef]
107. Yang, W.; Xiao, G.; Zhu, Q.; Song, S.; Cao, G.-H.; Ren, Z. Effect of carbon doping on the structure and superconductivity in AlB_2-type $(Mo_{0.96}Ti_{0.04})_{0.8}B_2$. *arXiv* **2023**, arXiv:2302.14272. [CrossRef]
108. Lim, J.; Sinha, S.; Hire, A.C.; Kim, J.S.; Dee, P.M.; Kumar, R.S.; Popov, D.; Hemley, R.J.; Hennig, R.G.; Hirschfeld, P.J.; et al. Suppression of superconductivity in Nb-substituted MoB_2 at high pressure. *arXiv* **2023**, arXiv:2302.13936. [CrossRef]
109. Zhang, W.; Liu, X.; Wang, L.; Tsang, C.W.; Wang, Z.; Lam, S.T.; Wang, W.; Xie, J.; Zhou, X.; Zhao, Y.; et al. Nodeless superconductivity in Kagome metal CsV_3Sb_5 with and without time reversal symmetry breaking. *Nano Lett.* **2023**, *23*, 872–879. [CrossRef] [PubMed]

110. Troyan, I.A.; Semenok, D.V.; Ivanova, A.G.; Sadakov, A.V.; Zhou, D.; Kvashnin, A.G.; Kruglov, I.A.; Sobolevskiy, O.A.; Lyubutina, M.V.; Helm, T.; et al. Non-Fermi-liquid behavior of superconducting SnH_4. *arXiv* **2023**, arXiv:2303.06339. [CrossRef]
111. Jung, S.G.; Seo, S.; Lee, S.; Bauer, E.D.; Lee, H.-O.; Park, T. A peak in the critical current for quantum critical superconductors. *Nat. Commun.* **2018**, *9*, 434. [CrossRef] [PubMed]
112. Kim, Y.H.; Park, S.; Kwon, C.I.; Kim, S.Y.; Watanabe, K.; Taniguchi, T.; Kim, J.S. Two-dimensional multiband superconductivity of the optimally and uniformly Li-intercalated FeSe nanoflakes. *Curr. Appl. Phys.* **2023**, *46*, 27–33. [CrossRef]
113. Liu, X.; Zhang, W.; Lai, K.T.; Moriyama, K.; Tallon, J.L.; Yoshimura, K.; Goh, S.K. Peak in the critical current density in $(Ca_xSr_{1-x})_3Rh_4Sn_{13}$ tuned towards the structural quantum critical point. *Phys. Rev. B* **2022**, *105*, 214524. [CrossRef]
114. Nobukane, H.; Yanagihara, K.; Kunisada, Y.; Ogasawara, Y.; Isono, K.; Nomura, K.; Tanahashi, K.; Nomura, T.; Akiyama, T.; Tanda, S. Co-appearance of superconductivity and ferromagnetism in a Ca_2RuO_4 nanofilm crystal. *Sci. Rep.* **2020**, *10*, 3462. [CrossRef]
115. Jung, S.-G.; Han, Y.; Kim, J.H.; Hidayati, R.; Rhyee, J.-S.; Lee, J.M.; Kang, W.N.; Choi, W.S.; Jeon, H.-R.; Suk, J.; et al. High critical current density and high-tolerance superconductivity in high-entropy alloy thin films. *Nat. Commun.* **2022**, *13*, 3373. [CrossRef]
116. Li, C.; Zhao , Y.-F.; Vera, A.; Lesser, O.; Yi, H.; Kumari, S.; Yan, Z.; Dong, C.; Bowen, T.; Wang, K.; et al. Proximity-induced superconductivity in epitaxial topological insulator/graphene/gallium heterostructures. *Nat. Mater.* **2023**, *22*. *in press*. [CrossRef] [PubMed]